Lanthanum nickelate as an efficient oxygen electrode for solid oxide electrolysis cell

Fabrice Mauvy, Jean-Claude Grenier, Julien Vulliet, Aline Rougier, Jean-Marc. Bassat

Lanthanum Nickelate as Efficient Oxygen Electrode for Solid Oxide Electrolysis Cell

Fabrice Mauvy[1], Jean-Claude Grenier[1], Julien Vulliet[2] Jean-Marc Bassat[1], Aline Rougier[1,*]

[1]Université de Bordeaux, CNRS, Bx INP, ICMCB-UMR 5026, F-33600 Pessac, France.

[2]CEA, DAM, Le Ripault, F-37260 Monts, France

[*]Corresponding author: aline.rougier@icmcb.cnrs.fr

Abstract

The present study focuses on an alternative structured oxygen electrode for solid oxide electrolysis cell (SOEC). $La_2NiO_{4+\delta}$ nickelate, LNO, was selected with respect to its mixed electronic and ionic conductivity and its good chemical stability. Complete single cells were built using screen printing of LNO and $LaNi_{0.6}Fe_{0.4}O_3$ (LNF) layers on a standard hydrogen electrode supported half cell consisting of a porous NiO-YSZ layer, a dense 8YSZ electrolyte layer and a thin interlayer of GDC. The LNO cells polarization curves under various anodic flows of H_2O/H_2 (90/10) show excellent performances compared to the commercial LSCF ($La_{0.6}Sr_{0.4}Co_{0.2}Fe_{0.8}O_{3-x}$) based cells. The steam conversion ratio SC increases from around 40% to 80% when the gas flow decreases from 36 to 12 NmL min^{-1} cm^{-2}. With a degradation rate of 1.5% 1,000 hrs^{-1} after 500 hrs operating time (i = - 0.5 A cm^{-2}) at 800 °C, using a medium H_2O/H_2 (90/10) gas flow of 24 NmL min^{-1} cm^{-2}, LNO oxygen electrode shows higher durability than the state of the art LSCF oxygen electrode. Energy efficiency analysis confirms the dependency of the total efficiency with the current density and gas flow allowing us to suggest optimized conditions for reaching targets of commercial H_2 production.

Keywords ***:*** lanthanum nickelate, oxygen electrode, Solid Oxide Electrolysis Cell, aging, energy efficiency

1. Introduction

Nuclear energy systems usually operate at full capacity to produce electricity for grid base load power and the excess of heat and electricity should be recovered using an efficient way. For instance, the production of hydrogen (H_2) as clean and renewable commodity for storing energy can be largely promoted through the high temperature steam electrolysis (HTSE) [1]. Indeed, for large-scale H_2 production, high-temperature solid oxide electrolysis cells (SOECs) technology is considered as quite efficient [2-4]. However, to operate at high temperature, the SOEC components must meet some basic requirements for efficient and cost-effective hydrogen production, typically a good chemical stability in highly reducing/oxidizing environments and low reactivity *versus.* ageing. Yttria Stabilized Zirconia (YSZ) appears to be the most suitable electrolyte having a high ionic conductivity and being low cost. Ni–YSZ cermet as hydrogen electrode material and LSCF ($La_{0.6}Sr_{0.4}Co_{0.2}Fe_{0.8}O_{3-x}$) as oxygen electrode material are most widely used and commercially available [5]. However, during long-term operation, a degradation of LSCF is observed due to Sr and Co depletion [6]. Hence, Sr and Co-free alternative anode materials, such as $Ln_2NiO_{4+\delta}$ (Ln = La, Nd, Pr) nickelates, have attracted the interest of researchers with regard to their good mixed ionic electronic conducting (MIEC) properties [7-11]. Indeed, these materials show high electronic and O^{2-} ionic conductivities and large oxygen surface exchange rates inducing excellent electrochemical properties for oxygen electrode applications [12-17]. An interesting feature of these compounds is the presence of additional oxygen in the layered structure leading to oxygen overstoichiometry (δ), which makes them chemically stable over a wide range of temperature and oxygen partial pressure pO_2 [18-21]. Even though the praseodymium nickelate $Pr_2NiO_{4+\delta}$ exhibits the best performances, $La_2NiO_{4+\delta}$ (so-called LNO) appears the most stable material for use as an alternative oxygen electrode material for SOECs, especially with regard to aging [22-23]. This study aims to investigate and to highlight the performance of LNO as oxygen electrode in complete single cell in HTSE mode and to compare its behavior to the commercial anode material LSCF.

2. Experimental

2.1 Powder preparation and cell manufacturing

High purity powders of LNO were prepared via the citrate–nitrate route (modified Pechini method previously described in ref. [9]) starting from the precursors La_2O_3 (Strem Chemical, 99.99%), and $Ni(NO_3)_2.6H_2O$ (Acros Organics, 99%). The lanthanide oxide, La_2O_3, was pre-fired at 900 °C overnight to remove the water content because of its highly hygroscopic nature. After the combustion step of the nitrate–citrate mixture, an annealing at 1200 °C for 12 hrs in air was carried out. Single and well crystallized phase was obtained as confirmed by X-ray diffraction.

Figure 1 shows a schematic view of the Ni-YSZ supported single cell. Planar hydrogen electrode supported half-cell (60 mm in diameter) was prepared by tape-casting for the support and by screen-printing for the H_2 electrode functional layer and the electrolyte. The support was a 400 µm thick porous Ni-YSZ layer, the H_2 functional layer was a 20 µm thick porous composite of nickel oxide and yttria-stabilized zirconia (NiO-YSZ) and the electrolyte was a 10 µm thick dense (98%) 8YSZ layer. NiO-YSZ and YSZ were sintered at 1400 °C during 5 hrs. The NiO/YSZ ratio was 66/34 wt.%. After reduction the porosity of the functional layer was close to 25%. The H_2 electrode was reduced during 6 hrs before electrochemical measurements. A 3 µm thick barrier layer of Gadolinia Doped Ceria, $Ce_{0.8}Gd_{0.2}O_{1.9}$, GDC was coated by screen-printing to limit the chemical reactivity between the electrolyte and the O_2 electrode.

Terpineol-based LNO inks, containing 70% of active materials, were screen-printed on top of the GDC interface layer and sintered at 1200 °C, for 1 hr, in air, with a heating rate of 2 °C min^{-1}, leading to layers of about 20 µm thick. The GDC interfacial layer and oxygen electrodes were respectively 55 and 20 mm in diameter, to use the edge of the cell for sealing. An additional layer of $LaNi_{0.6}Fe_{0.4}O_3$ (LNF) was screen printed on LNO cell. This material was used as a collecting layer in order to improve the overall current collection. As previously shown [24], this material does not participate to the oxygen electrode reaction. It was *in situ* sintered in the electrochemical measurements setup at 900 °C for 2 hrs. These sintering temperatures were previously optimized to obtain a controlled homogeneous porous electrode microstructure corresponding to the lowest polarization resistance R_p values observed for LNO, (i.e., $R_p < 0.10$ Ω cm^2 at 800 °C) [25].

2.2 Electrochemical Measurements

Electrochemical characterizations were performed in a homemade set-up. In each experiment, cells were mounted and sealed to a metallic housing, providing gas flow channels and electrical

connections. Anodic and cathodic gases were introduced at the cell center and distributed onto the electrodes. A glass seal was deposited on the edge of the cell to ensure a complete gas tightness of the hydrogen compartment. Platinum and nickel grids were used for the electrical contact (100 mesh cm^{-2}), enhanced by a mechanical pressure of 400 g cm^{-2} applied on the set-up. Steam was produced by burning the appropriate H_2/O_2 ratio in a specific chamber before feeding the cell. All the measurements were conducted using a Solartron potentiostat/impedance frequency analyzer (MODULAB with specific HV100 and FRA modules equipped with a booster 12 V 20 A). At the operating temperature and for the different gas feeding conditions, the polarization curves were recorded in galvanodynamic mode (20 mA s^{-1}) from open circuit voltage (OCV) to 0.7 V in SOFC mode and starting from OCV to 1.4 V in SOEC mode. The cell aging was studied by recording the evolution of the voltage as a function of time in galvanostatic mode. Current density-voltage and power density curves were recorded at 800 °C in SOFC and SOEC modes. For SOFC mode the hydrogen flow (pure H_2) was 24 NmL min^{-1} cm^{-2} while in SOEC mode the gas flow of H_2O/H_2 (90/10) mixture varies from 12 to 36 NmL min^{-1} cm^{-2}. The cell aging in SOEC mode was measured at 800 °C under a current density of -0.5 A cm^{-2} and a gas flow of 24 NmL min^{-1} cm^{-2}.

3. Results and Discussion

3.1 Start-up procedure

The test procedure started by heating the cell (under N_2/H_2 mixture for the H_2 side and air for the O_2 side) at a rate of 1 °C min^{-1} up to 920 °C during 30 minutes (glass sealing treatment). After that, the temperature was lowered to the operating temperature, namely 800 °C, and the NiO/YSZ electrode was reduced by progressively increasing the hydrogen amount in the gas stream. The H_2 electrode side was finally fed with only hydrogen gas using a flow of 24 NmL min^{-1} cm^{-2}. The corresponding oxygen partial pressure was considered close to $p(O_2) = 5\times10^{-24}$ bar. The OCV was measured in these conditions to evaluate the quality of the electrolyte tightness, and the correct formation of the glass seal before recording polarization curves in fuel cell mode (see Figure 2). Using the Nernst equation, a theoretical OCV value of 1.204 V was calculated. The closeness of the experimental OCV value (1.199 V) to the theoretical one validates the sample cell and the assembly in the testing set-up. In addition, the total Area Specific Resistance value of the cell (ASR_{tot}) under operation determined in the linear domain (in the range 0.9 – 0.7 V) was estimated at 0.285 Ω cm^2. This relatively low value allowed concluding that the CERMET NiO/YSZ reduction process is satisfying and the cell is ready to

be operated in the electrolysis mode. After these different steps, the cell was then fed by a H_2O / H_2 (90 /10) flow for experiments in electrolysis mode.

3.2 Electrochemical measurements in HTSE mode

At first, the OCV was measured in HTSE mode for various H_2O/H_2 flows (12 to 36 NmL min $^{-1}$ cm^{-2}). Compared to the theoretical value, 0.840 V, the determined experimental OCV values showed a relative difference, $\Delta OCV = (OCV_{exp.} - OCV_{th.}) / OCV_{th.}$, lower than 1.7%, whatever the selected flow value (Table 1). Then, the polarization curves i-E in electrolysis mode were recorded for these three H_2O/H_2 flows. The data are plotted in Figure 3. The curves can be divided in three parts: in the low current density range (- 0.20 $<$ i $<$ 0 A cm^{-2}), the cells show a quasi nonlinear behavior. In the intermediate range, an ohmic-type behavior is observed in a large domain for the highest flow value, while for lower flows, they diverge from linearity at increasing current density absolute value, the linear part being quite limited when the flow is 12 NmL min^{-1} cm^{-2}. For an operating potential of 1.3 V corresponding to almost the auto thermal regime (ΔH = 247.9 kJ mol^{-1}/2F), the current density is in the range -1.18 to -1.67 mA cm^{-2} as reported in Table 2. These values are rather close to the current density obtained with a similar cell using LSCF as anode material and operating in the same conditions (12-36 NmL min^{-1} cm^{-2}). Concerning the highest current density, a limiting current density can be noticed. Because this limit regime seems to appear for lower current when the supplying flow is lower it can be deduced that the mass transport (water vapor diffusion) is the limiting step and a steam depletion could be present at the electrode surface at the cathode side. These results allow to conclude on the good performance of the cell based on this anode architecture.

Considering a faradic efficiency equal to 1, the steam conversion ratio SC can be calculated from the operating current density divided by 2F according to the chemical reaction

$$H_2O + 2e^- \rightarrow H_2 + O^{2-} \quad (1)$$

and also the water vapor flow (taking into account that the gas mixture is 90% of water and 10% of hydrogen). As expected, the highest SC values are obtained for the lowest gas flow (around 82% for 12 NmL min^{-1} cm^{-2}) and the SC drastically decreases when the gas flow increases (around 38% for 36 NmL min^{-1} cm^{-2}).

The nonlinearity of the i-E curves observed in the current density range (- 0.20 $<$ i $<$ 0 A cm^{-2}) (so called low regime), may be reasonably assigned to the electrolysis current that causes an increase in $p(O_2)$ at the air side, close to the electrode surface. It results in both an increase of the electronic and ionic conductivities directly correlated to an increase of the Ni^{3+} amount (i.e.,

hole concentration) and additional oxide ions (i.e., increase in δ value). Such a behavior has been earlier reported by Kim et al. [26].

The values of the total ASR of the cell ($ASR_{tot.}$) evaluated from the dE/di in the linear domain (intermediate regime) of the i-E curves (see Figure 3), are reported in Table 3. The $ASR_{tot.}$ value slightly decreases from 0.36 down to 0.25 Ω cm^2 when increasing the steam flow rate from 12 to 36 NmL min^{-1} cm^{-2}, respectively. These low values confirm the good performances of this cell in HTSE mode. A typical Electrochemical Impedance Spectroscopy (EIS) diagram measured under working atmospheres at 800 °C for the HTSE cells and at OCV is reported in Figure 4. Using such Nyquist plots, the intercepts between the impedance data and the real axis allow to deduce the series resistance $R_{S(el+cc)}$ and total ASR_{tot} at high frequency and low frequency, respectively. Assuming that the total $ASR_{tot.}$ is the addition of the anode, electrolyte, cathode and current collectors impedance, one can analyze the relative contribution of each element at 800 °C. Indeed, the oxygen electrode polarization resistance $R_{P(ox.)}$ (LNO) was previously measured at 800 °C, in air, under zero dc conditions, and is close to 0.10 Ω cm^2 [27]. The ohmic resistance of the electrolyte and current collectors ($R_{S(el + cc)}$) was measured around 0.13 Ω cm^2 using EIS. It can be mentioned here that the resistances values measured under zero dc conditions have been extrapolated under current. This hypothesis agrees with the high stability of the electrolyte and oxygen electrode impedances reported by previous authors [28]. Thus, by subtracting these contributions to the total resistance, $ASR_{tot.}$, the hydrogen electrode resistance $R_{P(hy.)}$ can be deduced. The data are reported in Table 3. The $R_{P(hy.)}$ contribution decreases with the steam flow supplying the electrode. Indeed, the more the active species (H_2O) flow increases, the more the associated ASR at the hydrogen side decreases. For LNO, one should stress that for the lower gas flow rate, involving a high steam conversion, the hydrogen electrode contribution is much larger (around 36%). In such operating conditions, the oxygen electrode is no longer the most penalizing element of the cell ($Rp_{(ox.)}$ around 28%). A similar behavior is observed for LSCF based cell, confirming that the oxygen electrode is not always the most penalizing element of the cell, especially for high steam conversion ratios.

It is worthwhile comparing our results with those reported by Kim et al. [26] for similar cells, either with LSCF or LNO air electrodes, the current collector being a Pt mesh instead of LNF oxide. At 800 °C, the total ASR was 0.32 Ω cm^2 for LSCF and 0.43 Ω cm^2 for LNO, the flow rate of fuel consisting of 80% H_2O/20% H_2 of 100 NmL min^{-1} cm^{-2} was much higher than ours

and the air electrode was exposed to open air. The LNO electrochemical cell tends to show better performances, probably due to an optimized cell manufacture. Both results confirm the promising properties of the lanthanum nickelate as efficient oxygen electrode material in SOEC.

3.3 Aging study under polarization

With regard to these good results of both cells in HTSE mode, the next step was to evaluate the aging issue. The selected operating conditions for that was a medium flow of 24 NmL min^{-1} cm^{-2} and a current density -0.5 A cm^{-2} (galvanostatic mode). Using these operating conditions, the steam conversion rate (SC) is close to 30%. The recorded voltage *versus* time (over 500 hours) is reported in Figure 5. The variation of voltage upon time shows a small decrease prior to an increase after about 50 hrs to finally reach a stabilization leading to a relative variation of around 1.5 % 1,000 hrs^{-1} after 500 hrs operating time. In comparison, the degradation is larger for cells with the LSCF oxygen electrode: during 250 hrs, the relative variation of voltage is around 2% 1,000 hrs^{-1}, then, it increases, being more than 4% 1,000 hrs^{-1} after 450 hrs. X-ray characterizations on both oxygen electrodes after aging show no evolution of the LNO electrode while extra $SrCrO_4$ phase was detected in addition of LSCF. The long-term stability issues such as surface segregation of Sr during operation in LSCF is a well-documented phenomenon and a larger description is not the purpose of this paper. The absence of structural changes in LNO oxygen electrode after aging is in good agreement with its behavior in single cells as reported by Vibhu et al. [23]. For both oxygen electrodes, SEM analysis of the aged cells shows no major microstructure changes before and after aging as well as no clear evidence of adhesion loss in between the LNO electrode and the GDC electrolyte (See Figure 6). The purpose of this paper being the electrochemical investigation of LNO cells with comparison with LSCF cells, preliminary post-aging structural characterizations need to be deeper analyzed in the future.

3.4. Energy efficiency analysis

Even though the previous results suggest that the highest performances, in terms of current density-potential values, are obtained for a steam flow of 36 NmL min^{-1} cm^{-2}, it is relevant to evaluate the energy balance of these cells. The aim of this study is to determine the optimized operating conditions with respect to the steam flow and (i, E) parameters, starting from thermodynamic and polarization curves data.

The energy efficiency rate of a water electrolysis cell can be defined as the ratio of the energy produced by di-hydrogen gas combustion (low heating value, LHV) over the electrical energy amount injected to the cell to split the water molecules (current density $i \neq 0$) under constant (T, p) operating conditions.

The total efficiency ρ_{Tot} can be defined using the following equation [29]:

$$\rho_{Tot.} = \rho_{Thermo.} \times \rho_{Voltage} \times \rho_{Faradic} \times SC \quad (2)$$

where:

(i) ρ_{Thermo} is the thermodynamic efficiency, which is defined as the ratio between the total enthalpy for water splitting (ΔH) and the free enthalpy (ΔG) at the operating temperature, i.e., $\rho_{Thermo} = \Delta H_{op.} / \Delta G_{op.}$. For T = 800 °C, their values are extracted from ref. [30]: $\Delta H_{op.}$ = 247.9 kJ mol^{-1} and $\Delta G_{op.}$= 188.1 kJ mol^{-1}. The value of ρ_{Thermo} is then equal to 1.318. Such a high value (> 1), can be obtained because heat from the environment is transferred to the system during electrolysis operation, which can theoretically enable the production of more chemical energy of hydrogen fuel than the electrical energy supplied for the electrolysis process.

(ii) $\rho_{Voltage}$ is the voltage efficiency. This term can be calculated using the ratio between the theoretical value of the open circuit voltage (OCV) (for given T and p(H_2, H_2O and O_2)) and the real voltage of the cell under operating conditions E(i): $\rho_{Voltage}$ = OCV / E(i). The reaction of water electrolysis being an endothermal process ($\Delta H_{op.} > 0$), thus, three operating modes can be distinguished as a function of the cell potential. At 800 °C, the thermodynamic potential of the reaction is close to 1.3 V: it corresponds to the so-called auto-thermal mode. For this specific potential value, the heat generated by the internal cell resistance is equal to the heat consumed by the electrolysis reaction. At a lower potential, heat must be externally supplied to maintain the system at a constant temperature, it is the endothermal mode. For cell potentials higher than 1.3 V, heat is generated by the internal cell resistance. (i.e., the Joule effect), the cell operates in the exothermal mode (it can be noted that this additional heat can be used to preheat the incoming gases at the system level).

For T = 800 °C and a cell fed in HTSE mode by a H_2O/H_2 (90/10) flow, the OCV is 0.840 V. The calculation was performed for the operating conditions, $E_{op.}$ = 1.3 V, and the corresponding current densities, $i_{op.}$, whose values are given in Table 4. It must be mentioned that these operating conditions have been considered in the intermediate regime, i.e., in the linear domain

(ohmic domain) of the polarization curve (i, E). No mass transfer limitation or charge transfer activation regime has to be considered in these selected conditions.

(iii) $\rho_{Faradic}$ is the ratio between the produced di-hydrogen amount versus the number of electrons injected in the cell. As currently observed with such HTSE cells, the ionic transport number of the ceramic membrane (YSZ) is close to one under the selected operating conditions (i.e., temperature, anodic and cathodic oxygen partial pressures, voltage and current density), then one can consider that $\rho_{Faradic} = 1$ [31].

(iv) SC represents the Steam Conversion as defined before. Concerning the fuel cell mode, the Fuel Utilization ratio (F.U. being the ratio between the theoretical H_2 flow deduced from the electrical current and the experimental H_2 injected flow) must be considered (see Table 4).

Using equation (2), the total efficiencies calculated for LNO and LSCF based SOECs are reported in Figure 7 *versus* the applied current density for different steam flows. As expected, three different regimes can be distinguished according to the values of the current density. For low negative current densities, so-called "low regime", from 0 to - 0.5 A cm^{-2}, the total efficiency is limited by the low steam conversion ratio whatever the selected flow. At increasing negative current density, it is mainly governed by the voltage efficiency. For all the curves, in the high current density range, a maximum efficiency seems to be reached being a compromise between the contribution of these two parameters (SC and $\rho_{Voltage}$) (i.e., $\rho_{Tot} = 69.3\%$ at i = - 1.28 A cm^{-2}, $\rho_{Tot.} = 47.2\%$ at i = - 1.71 A cm^{-2} and $\rho_{Tot.} = 35.7\%$ at i ≈ - 1.98 A cm^{-2} for 12, 24, 36 NmL min^{-1} cm^{-2}, respectively). Considering the only SOEC unit cell without taking into account auxiliary units, it can be concluded that an optimum efficiency is obtained using low steam supplying flow in association with a high (and adjusted) current density. Concerning the steam conversion ratio, the associated values are rather high: 81.5%, 51% and 38% for the 12, 24 and 36 NmL min^{-1} cm^{-2} flows, respectively. These raw SC values are in the range currently required for industrial application.

In addition, it can be noticed that the corresponding operating voltages, *i.e.* E_{op} = 1.395 V, 1.383 V and 1.391 V, for 12, 24 and 36 NmL min^{-1} cm^{-2}, respectively, are slightly higher than the thermo-neutral potential (1.285 V). It means that the cell would operate in the exothermal mode for which heat is generated by the internal cell resistance (i.e., Joule effect).

At this stage, the thermal operating conditions have to be discussed. Indeed, regarding the cell efficiency, a key point to consider is the energy associated to maintain the device at the operating temperature, i.e., 800 °C. In the previous calculation of $\rho_{Tot.}$, the thermal energy necessary to heat and maintain the system at 800 °C was not taken into account. To consider this additional contribution, the thermal energy ($T.\Delta S$) should be introduced in the calculation using data of ref. [30], i.e., $T.\Delta S$ = - 59.5 kJ mol^{-1}, i.e., 0.308 V, which leads to calculate the global efficiency # 2, $\rho_{Glob.}$. All the data and results are gathered in Table 4. The evolutions of $\rho_{Tot.}$ and $\rho_{Glob.}$ *versus* the current density are reported for both cells in Figure 8. Such an analysis could be an interesting tool to help the operator to better identify the most appropriate operating conditions of the electrochemical cell (and according to the complete electrolysis system).

For both oxygen electrode materials, the efficiencies are very similar whatever the current density. As expected, when the thermal energy is considered the total efficiency is reduced up to ≈ 7% depending on the current density, *i.e.* the steam conversion ratio. According to the calculated efficiencies #1 and #2 reported in Table 4 at the thermo-neutral operating point (≈ 1.3 V), a strong influence of the supplying steam flow on the efficiency can be observed. In the investigated current density range (i.e., $-2 < i$ (A cm^{-2}) < 0), a low supplying flow allows improving drastically the energy efficiency.

In Table 4, the HTSE and SOFC modes are reported using a similar flow. First of all, from these data, it can be noticed that operating in the high temperature range, i.e., 800 °C, is very interesting for both HTSE and SOFC modes from a pure thermodynamic viewpoint because ρ_{Thermo} stays high. Nevertheless, considering kinetic issues and under "classical" voltage operating conditions (i.e., 1.3 V and 0.7 V for HTSE and SOFC modes, respectively), the efficiency drastically decreases down to 43.5% for HTSE and 15.3% for SOFC mode (using the same supplying flow of 24 NmL min^{-1} cm^{-2}). In the HTSE mode, even if the oxidation-reduction reaction is theoretically endothermic in the low potential range, in practice, the electrolysis reaction will be exothermic in the operating condition because of various losses which have almost the same nature as in the fuel cell mode: activation and diffusion losses, and ohmic drop. In addition, when the thermal energy necessary for such high temperature conditions is taken into account, the total efficiency is again reduced. It is finally close to 56.1% for a water vapor flow of 12 NmL min^{-1} cm^{-2}.

According to studies dedicated to the complete HTSE systems (cf., Targets Europe [32]), a minimum steam conversion ratio close to 70% seems to be required for technical and economic reasons. Such a condition is obtained using the lowest water vapor flow (i.e., 12 NmL min^{-1} cm^{-2} and i ≈ -1 A cm^{-2}) whereas it is much more difficult to reach this target for a high flow range. As an example, a current density close to -3 A cm^{-2} with 36 NmL min^{-1} cm^{-2} would be necessary to reach a SC of 70%.

4. Conclusion

Herein, the promising properties of the MIEC oxide, $La_2NiO_{4+\delta}$, as oxygen electrode for SOECs are demonstrated through a careful analysis of its electrochemical properties. The polarization curves of LNF/LNO /GDC/8YSZ/ Ni–YSZ complete single cells, in HTSE mode, at 800 °C, show a strong dependence of the steam flow (H_2O/H_2 (90/10)), varying from 12 to 36 NmL min^{-1} cm^{-2}. In addition, from the determined ASRs, the contribution of each component of the cell is evaluated and it is clearly observed that the oxygen electrode is no more the most penalizing element at low flow rate. The comparison with LSCF based complete cells confirms the benefit of using LNO electrode: a degradation rate of 1.5 % 1,000 hrs^{-1} for 500 hrs aging is reported for LNO based complete cell under a medium flow of H_2O/H_2 (90/10) of 24 NmL min^{-1} cm^{-2} and a current density of - 0.5 A cm^{-2} (galvanostatic mode) whereas it is close to 4 % 1,000 hrs^{-1} for LSCF based cell. The water vapor conversion rate (SC) also strongly depends on the steam flow rate. Then, a careful analysis of the energy efficiency led us to suggest operating conditions to reach the maximum SC close to 70% required for technical and economical reasons. Such a condition is obtained using a low water vapor flow (i.e., 12 NmL min^{-1} cm^{-2} and a current density of i ≈ -1.15 A cm^{-2}).

Acknowledgments: The authors wish to thank Alexandre Kucharski for technical support, and the French ANR for financial support **_Grant Number ANR-13-PRGE-0008**

References

[1] R. Pinsky , P. Sabharwall , J. Hartvigsen , J. O'Brien, Prog. Nucl. Energy **2020**, 122(3), 103317.

[2] A. Brisse, J. Schefold , M. Zahid, Int. J. Hydrogen Energy **2008**, 33, 5375.

[3] J.-D. Holladay, J. Hu , D.-L.King, Y. Wang, Catal. Today **2009**, 139 (4), 244.

[4] M. Ni, M.-K.-H. Leung, D.-Y.-C. Leung, Int. J. Hydrogen Energy **2008**, 33, 2337.

[5] N. Mahato, A. Banerjee, A. Gupta, S. Omar, K. Balani, Prog. Mater. Sci. **2015**, 72, 141.

[6] C.E. Frey, Q. Fang, D. Sebold, L. Blum, J. Electrochem. Soc. **2018**, 165(5), F357.

[7] V. Kharton, A. Viskup, E. Naumovkh, F. Marques, J. Mater. Chem. **1999**, 9 (10), 2623.

[8] S.-J .Skinner, J.-A. Kilner, Solid State Ionics **2000**, 135(1-4), 709.

[9] E. Boehm, J.-M. Bassat J.M, P. Dordor, F. Mauvy, J.-C. Grenier, P. Stevens, Solid State Ionics **2005**, 176, 2717.

[10] A. Aguadero, L. Fawcett, S. Taub, R. Woolley, K.-T. Wu , N. Xu, J. Kilner, S. Skinner, J. Mater. Sci.**, 2012**, 47 (9), 3925.

[11] A. Aguadero, J.-A. Alonso, M. Martinez-Lope, M.-T. Fernandez-Diaz, M.-J. Escudero, L. Daza, , J. Mater. Chem. **2006**, 16 (33), 3402.

[12] F. Chauveau , J. Mougin, F. Mauvy, J.-M. Bassat, J.-C. Grenier, Int. J. Hydrogen Energy **2011**, 36, 7785.

[13] S. Choi, S. Yoo, J.-Y. Shin, , G. Kim, J. Electrochem. Soc. **2011**, 158, B995.

[14] T. Ogier, F. Mauvy, J.-M Bassat, J. Laurencin, J. Mougin, J.-C. Grenier, Int. J. Hydrogen Energy **2015**, 40, 15885.

[15] Y. Lee , H. Kim, Ceram. Int., **2015**, 41, 5984.

[16] A. Egger, N. Schrödl, C. Gspan, W. Sitte, Solid State Ionics **2017**, 299, 18.

[17] S. Saher, J. Song, V. Vibhu, C. Nicollet, A. Flura, J.-M. Bassat, H.-J.-M. Bouwmeester J. Mater. Chem. A **2018**, 6, 8331.

[18] M. Burriel, H. Tellez, R.-J. Chater, R. Castaing, P. Veber, M. Zaghrioui, T. Ishihara, J.-A. Kilner, and J.-M. Bassat, J. Phys. Chem. C **2016**, 120, 17927.

[19] J.-C. Grenier, F. Mauvy, C. Lalanne, J.-M Bassat., F. Chauveau, J. Mougin, J. Dailly, M. Marrony, ECS Trans. **2009**, 25(2), 2537.

[20] T. Nakamura, K. Yashiro, K. Sato, J. Mizusaki, Solid State Ionics **2020**, 181, 402.

[21] A. Flura A, S. Dru, C. Nicollet, V. Vibhu, S. Fourcade, E. Lebraud, A. Rougier, J.-M. Bassat, J.-C. Grenier, J. Solid State Chem. **2015**, 228, 189.

[22] Y.S. Yoo , M. Choi, J.-H. Hwang, H.-N. Im, B. Singh, S.-J. Song, . Ceram. Int. **2015**, 41, 6448.

[23] V. Vibhu, A. Flura, A. Rougier, C. Nicollet, J.-C. Grenier and J.-M. Bassat, J. Energy Chem. **2020**, 46, 62.

[24] C. Nicollet, A. Flura , V. Vibhu, A. Rougier, J.-M. Bassat, J.-C. Grenier, J. Power Sources **2015**, 294, 473.

[25] A. Flura, C. Nicollet, V. Vibhu, B. Zeimetz, A. Rougier, J.-M. Bassat, and J.-C.Grenier, J. Electrochem. Soc. **2016**, 163(6), F523.

[26] S.-J. Kim, K.-J. Kim, A.-M. Dayaghi, G.-M. Choi, Int. J. Hydrogen Energy **2016**, 41, 14498.

[27] T. Ogier, F. Chauveau, J.-M. Bassat, F. Mauvy, J.-C. Grenier, J. Mougin, M. Petitjean, ECS Transaction **2011**, 35, 1817.

[28] F. Shen, K. Lu, Fuel Cells **2018**, 18(4), 457.

[29] R.O'Hayre, Fuel Cell Fundamentals, 3rd ed., Wiley&Sons Inc, Hoboken, NY, USA, 2016, Ch.2, 60-65.

[30] Ruscic B. Active Thermochemical Tables: water and water dimer, The Journal of Physical Chemistry **2013**, 117, 11940.

[31] V. V. Kharton, F. M. B. Marques, A. Atkinson, Solid State Ionics **2004** 174, 135.

[32] Hydrogen Europe, Strategic Research and Innovation Agenda, Final Draft, July 2020 https://hydrogeneurope.eu/sites/default/files/20200703%20Final%20Draft%20updated%20SRIA%20HE-HER.pdf

Figure Captions

Figure 1 – Schematic description of the Ni-YSZ cermet supported single cell (F = 60 mm, CEA support)

.

Figure. 2 - Polarization curve and corresponding power density of the cell with $La_2NiO_{4+\delta}$, LNO, oxygen electrode, in SOFC mode, at 800 °C, under dry H_2 flow (24 NmL min^{-1} cm^{-2}) and air at the cathode side.

Figure. 3 - Polarization curves of cells with either LNO or LSFC as oxygen electrode in HTSE mode, at 800 °C, under various H_2O/H_2 (90/10) flows.

Figure 4 – Typical EIS diagram of the electrochemical cells measured at 800 °C under zero dc condition.

Figure 5 - Aging performance of the cell, with either LNO oxygen electrode or LSCF oxygen electrode in HTSE mode, at 800 °C, under H_2O /H_2 (90/10) flow of 24 NmL min^{-1} cm^{-2} and a current density of -0.5 A cm^{-2}.

Figure 6 - SEM images of aged cell with LNO oxygen electrode. A magnification of the cell is given on the right

Figure 7 - Dependence of the total efficiency on the current density for cells with LNO or LSCF oxygen electrodes in HTSE mode, at 800 °C, under various H_2O/H_2 (90/10) flows.

Figure 8 - Current density dependence of the calculated efficiencies $\rho_{Tot.}$ and $\rho_{Glob.}$ for cells with LNO or LSCF oxygen electrode in HTSE mode, at 800 °C, under a H_2O/H_2 (90/10) flow (36 NmL min^{-1} cm^{-2}).

Table 1 : Experimental OCV values recorded using various H_2O / H_2 flows (12 ; 24 ; 36 NmL min^{-1} cm^{-2}) and the relative difference $\Delta OCV/OCV_{th.}$ (%).

Flow / NmL min^{-1} cm^{-2}	$OCV_{exp.}$ / V	$(\Delta OCV)/OCV_{th.}$ / %
12	0.840	0
24	0.832	-0.95
36	0.826	-1.67

Table 2 : Current density i and steam conversion SC measured at 1.3 V

Cells / Gas Flow	i at 1.3 V / A cm^{-2}	SC at 1.3 V / %
LNO - 36 NmL min^{-1} cm^{-2}	-1.67	38.5
LNO - 24 NmL min^{-1} cm^{-2}	-1.48	51.1
LNO - 12 NmL min^{-1} cm^{-2}	-1.18	81.5
LSCF- 36 NmL min^{-1} cm^{-2}	-1.76	40.5
LSCF- 24 NmL min^{-1} cm^{-2}	-1.56	53.9
LSCF- 12 NmL min^{-1} cm^{-2}	-1.22	84.3

Table 3 : Total ASR of the cell, specific ASR of the different components and associated percentages

Gas Flow / NmL min^{-1} cm^{-2}	ASR_{tot} / Ω cm^2	$R_{P(ox.)}$ / Ω cm^2	Relative $R_{P(ox.)}$ %	$R_{S(el.+cc)}$ / Ω cm^2	Relative $R_{S(el.+cc)}$ %	$R_{P(hy.)}$ / Ω cm^2	Relative $R_{P(hy.)}$ %
LNO-12	0.36	0.10	27.8	0.13	36.1	0.13	36.2
LNO-24	0.29	0.10	33.9	0.13	44.0	0.06	22.0
LNO-36	0.25	0.10	40.0	0.13	52.1	0.02	8.0
LSFC-12	0.32	0.03	9.4	0.13	40.6	0.16	50.0
LSFC-24	0.25	0.03	12.0	0.13	52.1	0.09	36.0
LSFC-36	0.24	0.03	12.5	0.13	54.2	0.08	33.3

Table 4 : Energy efficiency of the cell under operating conditions ($E_{op.}$, $i_{op.}$ and gas flow supplying the cell): thermodynamic efficiency, voltage efficiency and total efficiencies without (#1) and with (# 2) external heating of the cell at 800 °C.

(*) F.U. : fuel utilization

Oxygen electrode	**LNO**	**LNO**	**LNO**	**LSCF**	**LSCF**	**LSCF**	**LNO**
Mode	**HTSE**	**HTSE**	**HTSE**	**HTSE**	**HTSE**	**HTSE**	**SOFC**
Gas flow /NmL min^{-1} cm^{-2}	12	24	36	12	24	36	24
$E_{op.}$ / V	1.3	1.3	1.3	1.3	1.3	1.3	0.7
$i_{op.}$ / A cm^{-2}	-1.179	-1.478	-1.673	-1.220	-1.562	-1.772	1.002
SC %	81.5	51.1	38.5	84.3	54.0	40.5	F.U.=34.8*
Thermodynamic efficiency %	131.8	131.8	131.8	131.8	131.8	131.8	75.9
Voltage efficiency # 1 %	64.6	64.6	64.6	64.6	64.6	64.6	58.1
Total efficiency # 1 , $\rho_{Tot.}$ %	69.4	43.5	32.8	71.8	45.9	34.5	15.3
Voltage efficiency # 2 %	52.2	52.2	52.2	52.2	52.2	52.2	46.3
Global efficiency # 2, $\rho_{Glob.}$ %	56.1	35.2	26.5	58.0	37.1	27.9	12.2

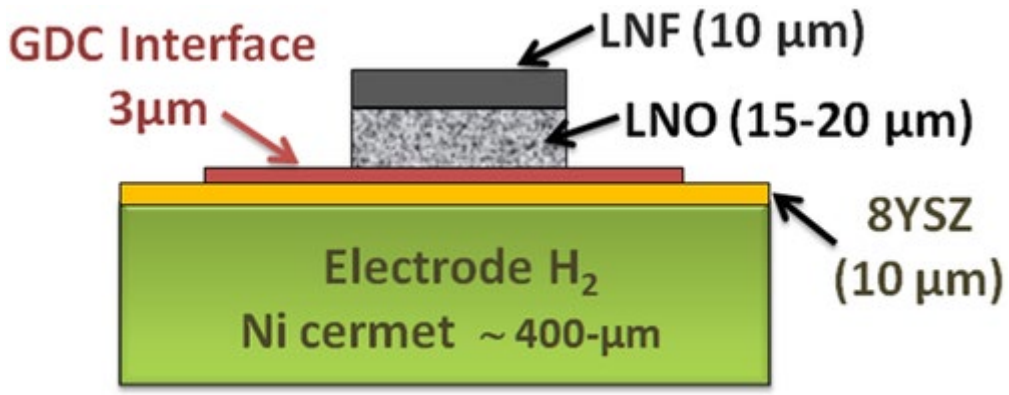

FIGURE 1

Schematic description of the nickel–Yttria-stabilized zirconia (Ni-YSZ) cermet supported single cell (*F* = 60 mm, CEA support)

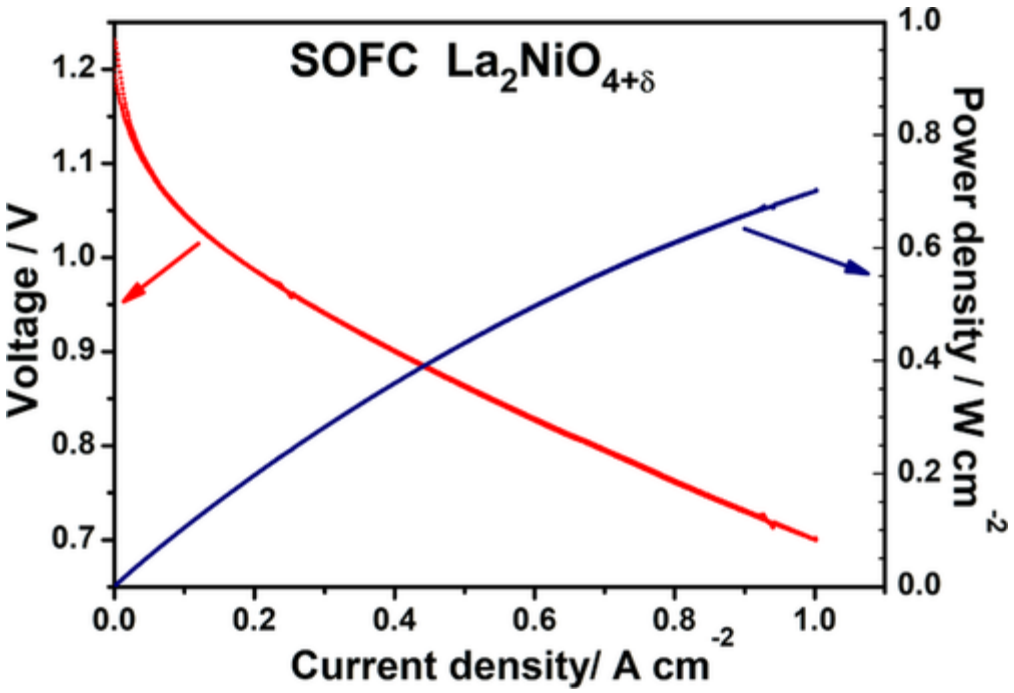

FIGURE 2

Polarization curve and corresponding power density of the cell with $La_2NiO_{4+\delta}$, LNO, oxygen electrode, in SOFC mode, at 800°C, under dry H_2 flow (24 N ml min^{-1} cm^{-2}) and air at the cathode side

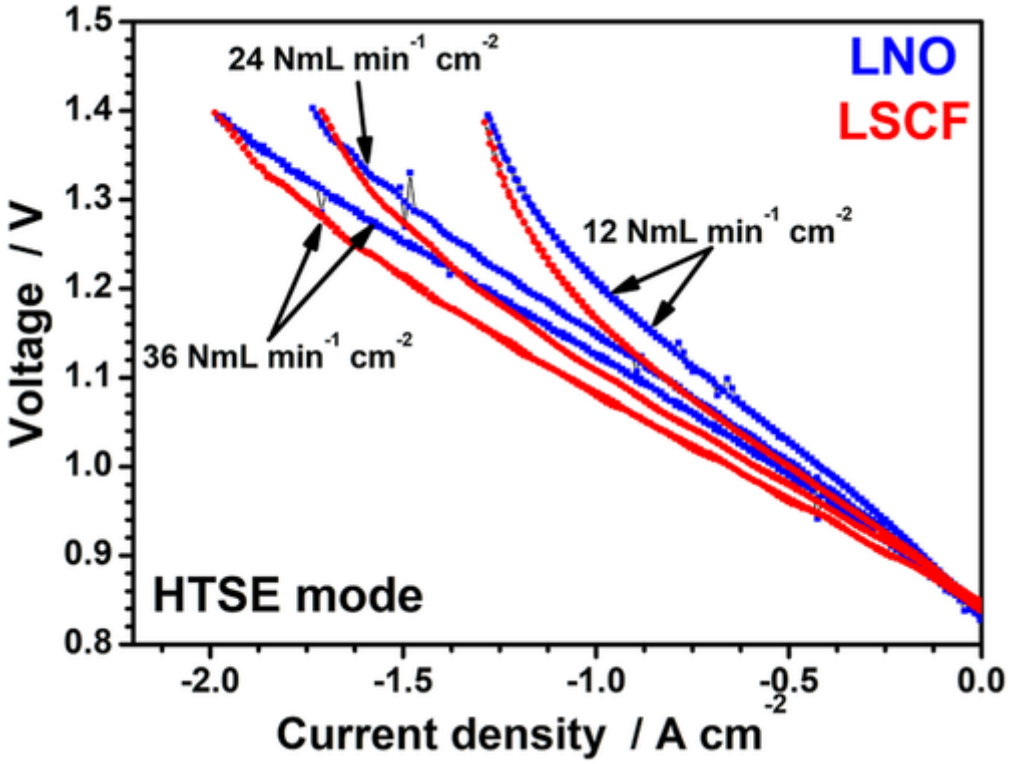

FIGURE 3

Polarization curves of cells with either LNO or LSCF as oxygen electrodes in high-temperature steam electrolysis (HTSE) mode, at 800°C, under various H_2O/H_2 (90/10) flows

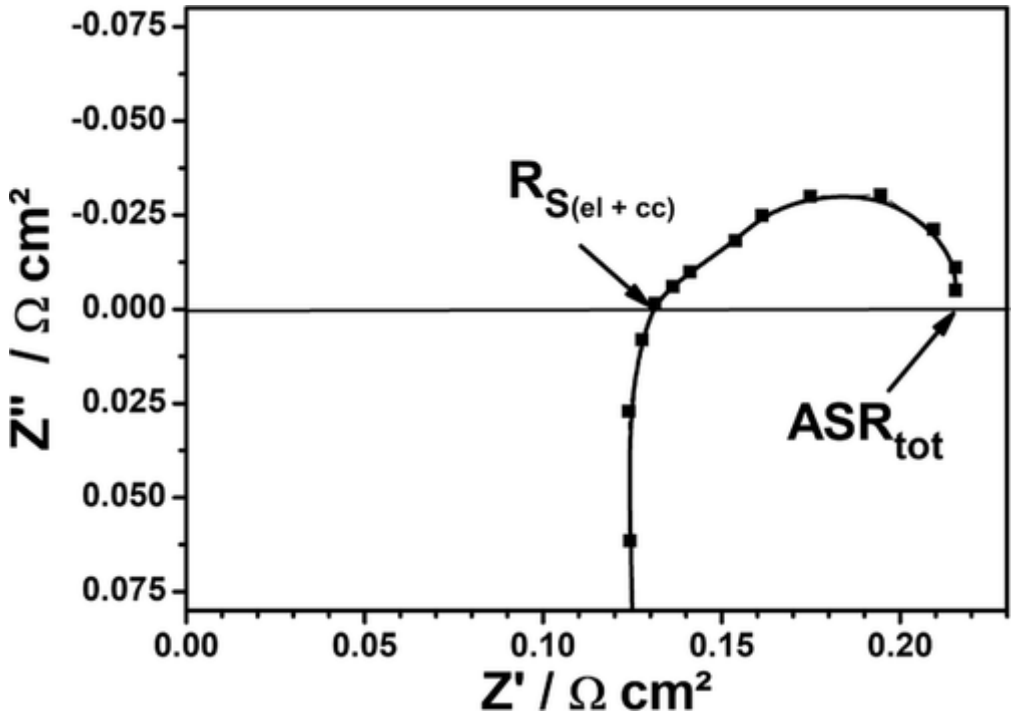

FIGURE 4

Typical electrochemical impedance spectroscopy (EIS) diagram of the electrochemical cells measured at 800°C under zero dc condition

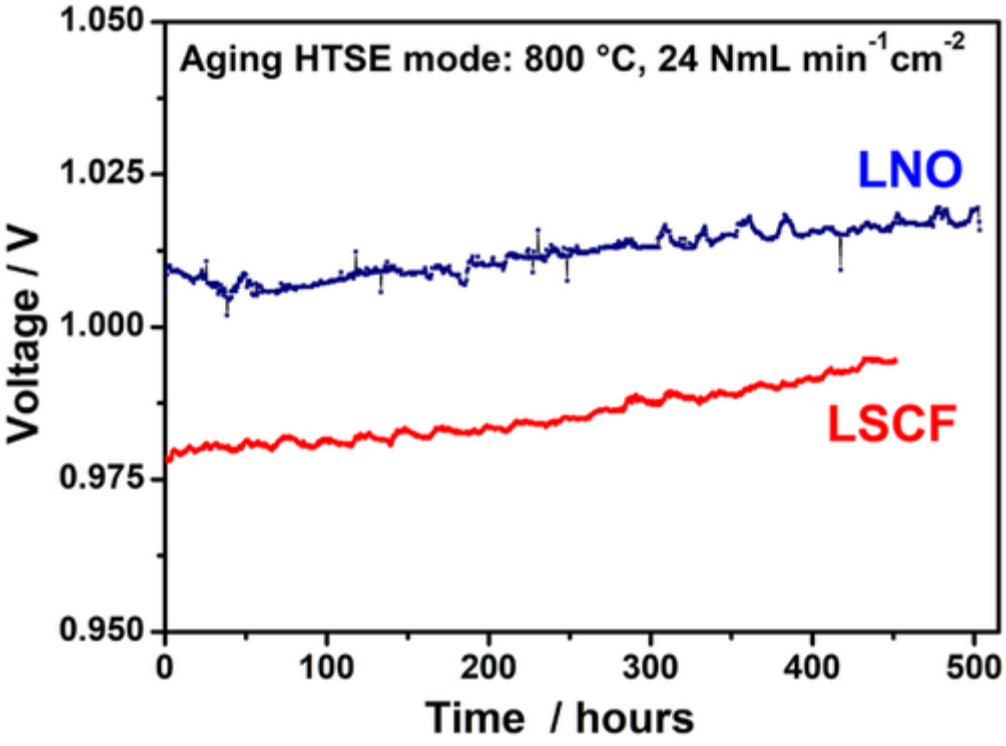

FIGURE 5

Aging performance of the cell, with either LNO oxygen electrode or LSCF oxygen electrode in high-temperature steam electrolysis (HTSE) mode, at 800°C, under H_2O /H_2 (90/10) flow of 24 N ml min^{-1} cm^{-2} and a current density of -0.5 A cm^{-2}

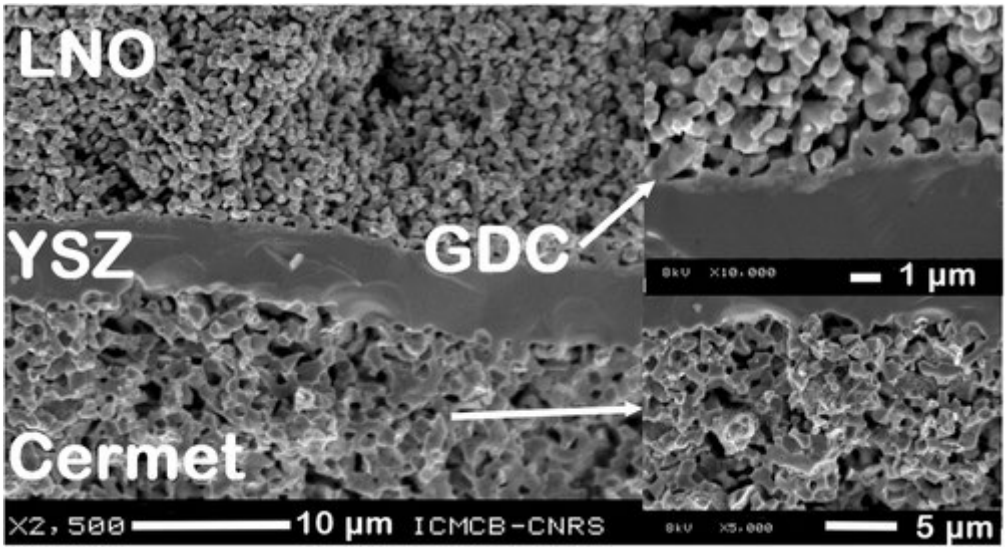

FIGURE 6

Scanning electron microscopy (SEM) images of aged cells with LNO oxygen electrode. A magnification of the cell is given on the right

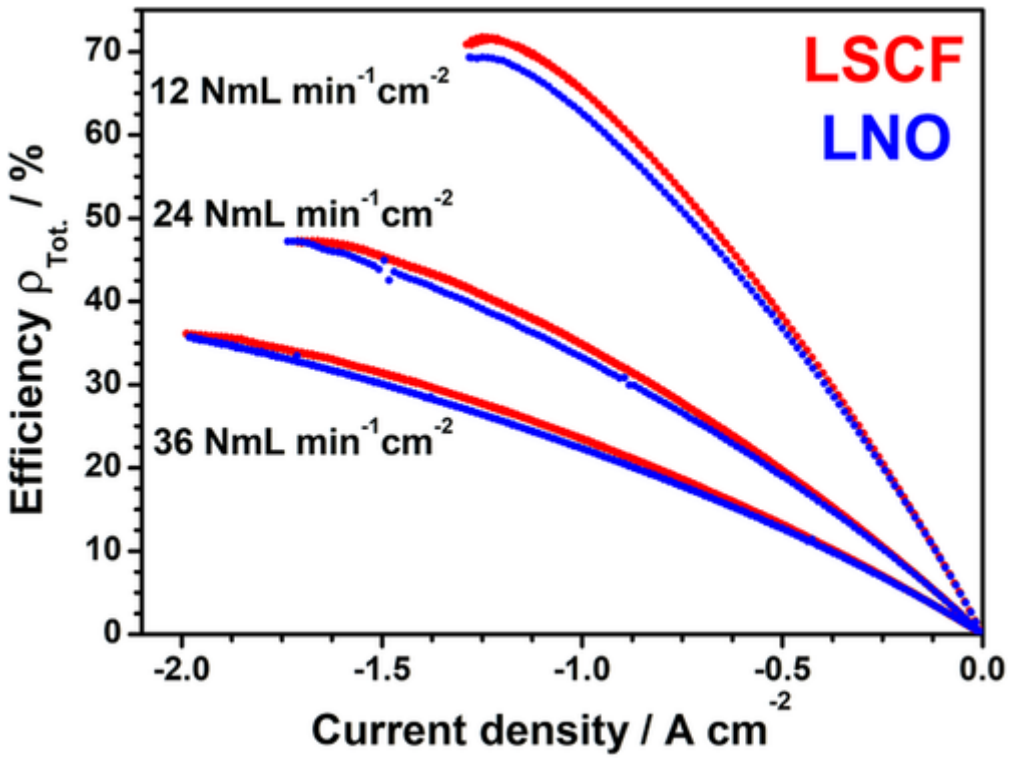

FIGURE 7

Dependence of the total efficiency on the current density for cells with LNO or LSCF oxygen electrodes in high-temperature steam electrolysis (HTSE) mode, at 800°C, under various H_2O/H_2 (90/10) flows

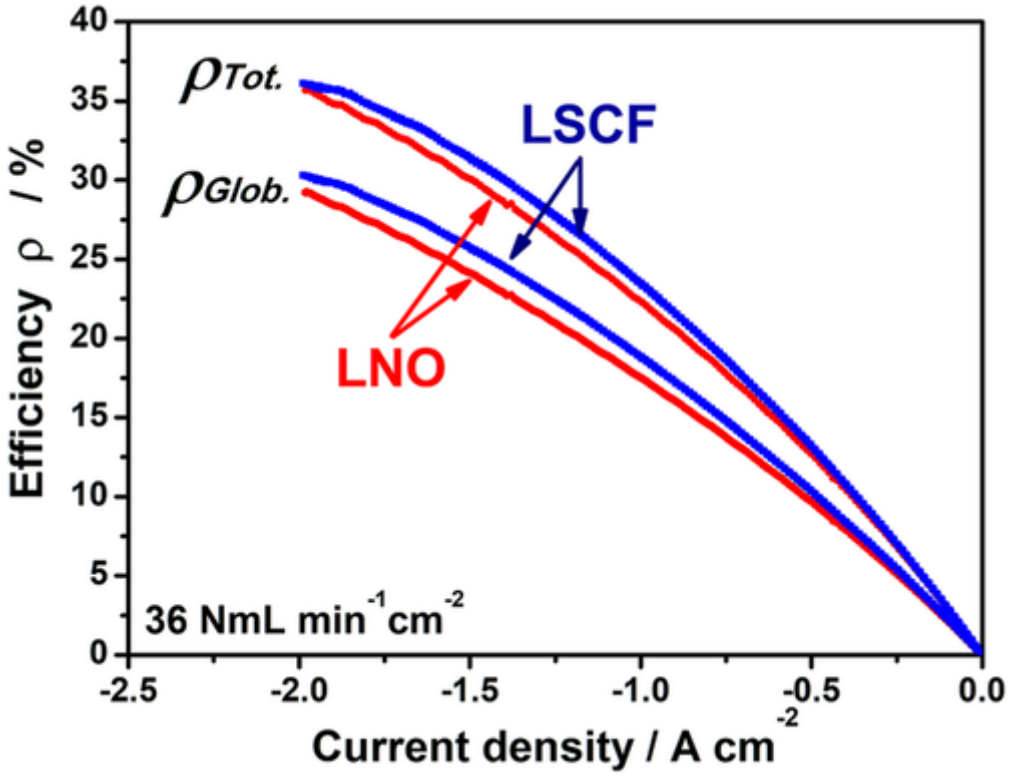

FIGURE 8

Current density dependence of the calculated efficiencies $\rho_{Tot.}$ and $\rho_{Glob.}$ for cells with LNO or LSCF oxygen electrode in high-temperature steam electrolysis (HTSE) mode, at 800°C, under an H_2O/H_2 (90/10) flow (36 N ml min^{-1} cm^{-2})